Ceramics International 51 (2025) 52662–52675

Contents lists available at ScienceDirect

Ceramics International

journal homepage: www.elsevier.com/locate/ceramint

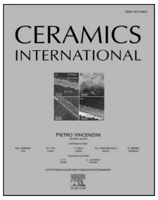

Advanced perovskite-BiZnB glass composite for electro-pyroprocessing salt waste streams: fabrication and chemical durability

Hao Ji [a], Kun Yang [a,b,*], Wangwei Ru [a], Yibo Wang [a], Ke Yang [c,**], Feida Chen [a,b], Chengying Bai [d], Xiaobin Tang [a,b]

[a] *Department of Nuclear Science and Technology, Nanjing University of Aeronautics and Astronautics (NUAA), Nanjing, 211106, China*
[b] *Key Laboratory of Advanced Nuclear Technology and Radiation Protection, Ministry of Industry and Information Technology, Nanjing, 211106, China*
[c] *Department of Materials Science and Engineering, The Hong Kong Polytechnic University, Hong Kong, China*
[d] *Department of Materials Science and Chemical Engineering, Harbin Engineering University, Harbin, 150001, China*

ARTICLE INFO

Handling editor: P. Vincenzini

ABSTRACT

The halide waste stream generated from advanced molten salt fast reactors and electro-pyroprocessing contain cumulative alkali and alkaline earth metal radionuclides and feature high environmental mobility, distinguishing it from the current waste stream. In this study, halide perovskite-derived $Cs_2NaInCl_6$ is fabricated as an ideal host material for the simultaneous immobilization of Cs, In, and Cl. Further, it is successfully incorporated into a self-assembled Bi-Zn-B glass with relatively low melting point (430 °C). The composite glass-ceramic waste form demonstrates relatively low processing temperatures, high waste-loading capacity, and excellent chemical durability, attributed to the gradual formation of the BiOCl passivation film, as confirmed by the semi-dynamic leaching curves. The stepwise phase degradation behavior is highly dependent on the chemical bonding environment that is dominated by an incongruent leaching mechanism and surface reorganization. The as-fabricated glass-ceramic waste form and proposed waste immobilization strategy provide a potential way to treat the questionable high-halide waste stream derived from electro-pyroprocessing and advanced molten salt reactors (MSRs).

1. Introduction

The electro-pyroprocessing of spent nuclear fuel make it readily compatible with advanced molten salt reactors (MSRs) because the uranium and transuranic elements are recovered at the cathode, while alkaline or actinides such as monovalent Cs, divalent Sr, and trivalent In, Nd, La, and Y primarily dissolve into the eutectic LiCl-KCl salt [1]. The eutectic LiCl-KCl salt requires periodical purification to separate it from the actinides to avoid a short current or other misfunctions in electrorefining [2–4]. Subsequently, the final waste stream featuring concentrated halide elements is immobilized, followed by geological disposal.

The intrinsic properties of metallic halides, namely high-water solubility as well as low melting and vapor point, pose significant challenges to the consolidation of waste streams. The radionuclides—strontium (Sr), barium (Ba), and cesium (Cs)—can be incorporated into the zeolite 4A $[Na_{12}(AlSiO_4)_{12}]$ obtained from the LiCl-KCl eutectic salt through ion exchange at approximately 425 °C followed by conversion to glass-bonded sodalite ceramic waste form ($Na_8(AlSiO4)_6Cl_2$) at 900 °C, achieving an immobilization ratio of approximately 8 wt% [3,5,6]. Leng et al. immobilized Cs and Sr using K-struvite crystals and chemically bonded phosphate ceramics under room temperature conditions, and investigated their interaction mechanisms via first-principles calculations [7,8]. Lead tellurite glass exhibits relatively low glass transition temperature ($T_g \sim 300$–400 °C), with a LiCl-KCl eutectic waste salt (ER (SF)) loading of approximately 15 wt% [9]. However, the tellurite glass has long been questioned for its low chemical durability, with corresponding cumulative normalized release rates of Cs, Cl, Te, and Pb, which are approximately 90, 500, 45, and 23 g/m^2, respectively, over an 11-d leaching period in deionized water at 90 °C.

The unique composition of metal halide double perovskites, including a tunable crystalline structure and significant proportion of halogens in the molecular structure, provides inherent advantages for immobilizing volatile radioactive halide salts, such as CsCl and CsI,

---

[*] Corresponding author. Department of Nuclear Science and Technology, Nanjing University of Aeronautics and Astronautics (NUAA), Nanjing, 211106, China.
[**] Corresponding author.

E-mail addresses: kun.yang@nuaa.edu.cn (K. Yang), keyanghnu@gmail.com (K. Yang).

https://doi.org/10.1016/j.ceramint.2025.09.024
Received 26 April 2025; Received in revised form 10 August 2025; Accepted 2 September 2025

which have been recognized as potential host materials for waste salts [10]. Scott et al. developed this approach as a potential method for the separation and solidification of radioactive waste by synthesizing Cs_2SnCl_6 through spark plasma sintering (SPS), and investigated its thermodynamic properties [11]. However, metal halide perovskite exhibits relatively poor thermal and chemical stability, making it unacceptable for long-term geological disposal [12,13]. Yang et al. developed composite and core-shell structures by incorporating the metal halide perovskite $Cs_3Bi_2I_9$ into chemically stable SiO_2 and hydroxyapatite, achieving a waste loading as high as 42 wt% for iodine and 14 wt% for cesium along with extremely low elemental release rates of 0.059 and 0.032 $g_N/m^2/d$ at 90 °C in deionized water, respectively [10,14]. The successful immobilization of halide perovskites is highly dependent on the vitrification point of the matrix material, which is restricted by the compatibility of the matrix material with halide perovskites. Therefore, it is necessary to explore novel matrix materials with low vitrification points and high chemical durability as alternatives for SiO_2 and hydroxylapatite.

Bismuth-based glasses with low glass transition temperature (T_g) and superior thermal stability have been extensively studied as low-melting-point glass binders or sealing materials [15–20]. Bismuth-based materials are also utilized as adsorbents to capture radioactive iodine or chloride by forming BiI_3 and BiOCl structures, which are environmentally stable according to DFT calculations [21–27]. Xian et al. demonstrated the use of Bi-B-Zn glass containing Bi_2O_3 to immobilize iodine-adsorbing Bi0-SiO_2 materials with an iodine retention ratio of 92.22 ± 2.6 % under N_2 sintering conditions [28]. Ri et al. optimized the Bi-Zn-B glass binder to achieve an iodine retention rate of 67 wt% in the glass matrix at sintering temperatures as low as 350–550 °C, with a corresponding I release rate lower than 1 g/m^2 [29].

In this study, a self-assembled Bi-Zn-B low-temperature glass matrix is synthesized with a metal halide double perovskite and is further incorporated in the formation of a dense glass-ceramic composite waste at a temperature of 430 °C and uniaxial pressure of 400 MPa. $Cs_2NaInCl_6$ and Bi-based glass can undergo a bonding reaction at relatively low temperatures, forming a stable BiOCl passivation layer, which enhances the chemical stability of the waste form. The chemical durability of the waste was evaluated using semidynamic leaching tests. The evolution of the microstructure and localized chemical bonding environment of the composite waste form was further characterized using in-situ Raman spectroscopy, X-ray diffraction (XRD), X-ray photoelectron spectroscopy (XPS), and scanning electron microscopy–energy dispersive spectroscopy (SEM-EDS). This study aims to provide mechanistic insights into the chemical durability of the waste form, contributing to the design and development of advanced glass-ceramic waste forms toward halide nuclide-bearing salt streams.

2. Materials and methods

2.1. Preparation of Bi-Zn-B low-temperature glass

High-polarizability cations, Bi_2O_3 and B_2O_3, were selected to act as the skeleton structure of the glass. The incorporation of Zn can significantly reduce the glass vitrification point, and consequently break down the Bi-B glass matrix. Therefore, in this study, a ternary glass of $30Bi_2O_3$-$55B_2O_3$-15ZnO (mol%) was prepared using the melt-quenching method. Powder of Bi_2O_3 (Macklin, 99.9 %), B_2O_3 (Macklin, 99.9 %), and ZnO (Macklin, 99.9 %) in stoichiometric ratios were thoroughly mixed using a corundum mortar and pestle. The mixture was then placed into a high-purity alumina ceramic crucible and calcined in a muffle furnace (SG-XS1700, Shanghai Sager Co., Ltd.) at 1100 °C for 2 h. The molten glass was quickly cast onto a stainless-steel mold preheated to 200 °C and subsequently annealed at 200 °C for 5 h to relieve thermal stress and strain.

2.2. Synthesis of $Cs_2NaInCl_6$ perovskite

$Cs_2NaInCl_6$ powder was synthesized via a solution-based method through the following reaction (1): CsCl (2 mmol, Macklin, 99.9 %) and NaCl (1 mmol, Macklin, 99.9 %) were dissolved in 3 mL of deionized water, and $InCl_3$ (1 mmol, Macklin, 99.9 %) was dissolved in 10 mL of warm HCl (80 °C). The CsCl/NaCl mixed solution was then added to HCl solution containing In^{3+} under vigorous stirring, forming a white precipitate. The reaction was allowed to proceed for 1 h to ensure completion. The mixture was subsequently filtered using filter paper with a pore size of 0.1 μm to obtain the $Cs_2NaInCl_6$ precipitate, which was then dried in a glove box for 24 h.The concentration of Cs ions in the residual solution, as determined by ICP analysis, was found to be less than 1×10^{-7} mol/L, which indicates that the Cs ions have been completely precipitated.

$$2CsCl + NaCl + InCl_3 \xrightarrow{HCl} Cs_2NaInCl_6 \quad (1)$$

2.3. Fabrication of composite waste form

Composite waste forms with halide perovskite compositions of 30, 50, and 70 wt% were prepared by mixing the $Cs_2NaInCl_6$ powder with Bi-Zn-B glass powder (Table 1) in a high-energy planetary ball mill (MITR-YXQM, Changsha MITR Co., Ltd) to reduce the particle size and increase the sintering ability (see Supplementary Fig. S1). The ball-milling speed was set to 500 rpm with five operational cycles, each consisting of 30 min of forward rotation and 30 min of reverse rotation. The milled powder was then subjected to rapid hot-press sintering.

The powder particles were sintered in a single step using an FHP-828 hot-press system (Shanghai Hateng Co., Ltd.) following the process outlined in Supplementary Fig. S2. For each sintering, approximately 2.4 g of the starting powder was loaded into a tungsten carbide (WC) mold. The inner surface of the mold was lined with 0.1-mm graphite paper to facilitate demolding after sintering. A thermocouple wire inserted 2 mm from the sample was used to measure the sample temperature. The sintering process was conducted under a vacuum of 1×10^{-2} MPa, applying uniaxial pressure at a controlled rate, with a maximum pressure of 400 MPa. The temperature was gradually increased to 430 °C at a rate of 50 °C/min and held at this temperature for 20 min, followed by natural cooling under vacuum. After sintering, the samples were polished with 0.25 μm diamond paste and ultrasonically cleaned with anhydrous ethanol. The polished samples were stored in a glove box for characterization and testing.

2.4. Microstructure characterization

The microstructure and crystalline structure evolution of the synthesized $Cs_2NaInCl_6$ powder and composite waste form before and after leaching test were evaluated by XRD with a PIXcel3D array detector receiver (PAN analytical, the NL), using a copper target (Kα = 0.15406 nm) at a step size of 0.013°. The surface morphology evolution of the samples was examined using a dual-beam ionization scanning electron microscope (TESCAN LYRA3 GM, CZ, USA) with an acceleration voltage of 10 keV. The phase distribution was observed in the BSE mode, and semi-quantitative elemental analysis was performed using an EDS system (Oxford Systems, UK). The Raman spectra of the synthesized $Cs_2NaInCl_6$ powder and the composite waste form before and after leaching were obtained using a Raman spectrometer (HORIBA HR

Table 1
Composition of raw materials and target element content (wt%) for composite.

	Glass	$Cs_2NaInCl_6$	Cs	Cl	In
1	70	30	12.9	10.4	5.6
2	50	50	21.6	17.3	9.3
3	30	70	30.2	24.2	13.0

Evolution, FR) with a 532-nm green laser with an exposure time of 10s and three accumulations. Thermogravimetric differential scanning calorimetry (TGA-DSC, STA 449 F3, GER) was employed to study the effect of the Bi-Zn-B glass on the thermal stability of the $Cs_2NaInCl_6$ perovskite. The chemical states of the elements before and after the leaching test were determined by XPS (ESCALAB Xi+, Thermo Fisher Scientific, USA), calibrated by C1s peak at 284.8 eV.

2.5. Semi-dynamic leaching tests

The chemical durability of the composite waste form was appraised by a semi-dynamic leaching test (ASTM C1308) [30] for 28 d at room temperature (RT) and 90 °C. The experiments were conducted in triplicate, following by taking average of the three parallel tests to ensure the data reliability. The samples were immersed in a PTFE-sealed vessel filled with deionized water (18 MΩ), and the leachates were exchanged at fixed intervals and with a constant surface area to solution volume (S/V) ratio of 5 m^{-1}. In each interval, 0.1 ml solution was diluted 100 times with 10 ml deionized water acidified with 8 % pure nitric acid, and its concentration was quantified using an inductively coupled plasma mass spectrometry (ICP-MS) system (ICAP6300, US).

The corresponding release rate of each element, m(i), in units of $mg\cdot m^{-2}\cdot d^{-1}$, is calculated using the following formula:

$$m(i) = \frac{C(i)V}{St} \times \text{Dilution factor} \tag{2}$$

where $C(i)$ is the concentration of different ions ($mg\cdot L^{-1}$) measured by ICP-MS, the dilution factor is 100, t is the sampling interval (d), V is the volume of the leachate (L), and S is the surface area of the sample (m^2). The surface area to volume ratio (S/V) is a constant 5 m^{-1}.

The normalized element release rate (L_N) is obtained using the following formula:

$$L_N = \frac{L}{\text{Weight percent}} \tag{3}$$

The cumulative quantity of the leached elements as a function of time was fitted using the Cote model, with the minimum R^2 achieved. The leaching kinetics of each element in the aqueous solution are described by the following empirical mathematical model:

$$M(t) = k_1 t + k_2 t^{1/2} + k_3\left(1 - e^{-k_4 t}\right) \tag{4}$$

where M(t) represents the cumulative leaching rate, expressed in mg/m^2; k_1t denotes the mass dissolution controlled by the dissolution behavior; $k_2t^{1/2}$ reflects the mass transport governed by the elemental diffusion; and $k_3(1\text{-}e^{-k4t})$ accounts for the mass exchange between surface defects and the solute in the solution. The long-term leaching rate can be derived by taking the derivative of the Cote model with respect to time and assuming that the leaching time approaches infinity, as denoted by k_1 [31].

2.6. MD calculation

Models of the $Cs_2NaInCl_6$/water interface were constructed using three MCl2 (M = Na, In) layers, where the double perovskite stabs were terminated by the MCl2 layers (Fig. 6). A $Cs_2NaInCl_6$ leaching environment, characterized by the experimental density of liquid water simulated by a vacuum region, was added on top of the perovskite stabs that were filled with water molecules for the $Cs_2NaInCl_6$ model.

All MD simulations of the Cs2NaInCl6 crystals in water were performed using the LAMMPS open-source package [32]. All equilibrated $Cs_2NaInCl_6$/water models were then equilibrated under the NVT ensemble by the Nose−Hoover thermostat and the Parrinello−Rahman barostat [33–35] at a constant temperature (T = 350 K) to accelerate the ion dissolution process. The dissolution rates of different elements (Cs^+, Na^+, $In3^+$, and Cl^-) were calculated by tracking the number of dissolved elements in liquid water based on a dissolution kinetics model.

3. Results

3.1. Microstructure, phase, and composition of the as-sintered composites

Fig. 1a shows the photographs of the as-fabricated low-temperature glass with variable ratios of Bi_2O_3, and the corresponding XRD profiles are shown in Fig. 1b. The color of the as-fabricated glass gradually darkened with the increasing Bi_2O_3 ratio, and high transparency was observed. The highly densified property without the manifested by-product of the glass was further confirmed by the SEM image in Fig. 1a. The amorphous property of the Bi-Zn-B glass was confirmed by the broadening of the XRD peaks at approximately 30° and 50°, which became increasingly pronounced with the increasing addition of Bi_2O_3. As shown in Fig. 1c, characteristic Raman peaks located at approximately 410, 592, 690, 880, 980, and 1340 cm^{-1} were observed for the as-fabricated glass with 20–40 mol% Bi_2O_3. Specifically, the Raman band at 410 cm^{-1} is assigned to the Bi-O-Bi stretching vibrations that occur between [BiO_3] and [BiO_6] polyhedral units [27], whereas the Raman band at 592 cm^{-1} can be attributed to the Bi-O stretching vibrations occurring within the [BiO_6] groups. In contrast, the Raman band at 690 cm^{-1} is attributed to the chain-type arrangements of the [BO_3] groups [36]. The Raman band at 880, 980, and 1300 cm^{-1} can be attributed to the pyroborate dimeric species [B_2O_5], orthoborate triangles [BO_3] [37], and B-O-B stretching vibrations occurring within the [BO_3] groups [38], respectively. The Raman vibrations associated with the [BiO_3] and [BiO_6] units at 410 cm^{-1} and 592 cm^{-1} gradually intensify with the increasing Bi_2O_3 composition, with a significant diminishing of Raman peak intensity occurring for [BO_3] and [B_2O_5], suggesting an increase in glassification due to the partial substitution of B_2O_3 by Bi. The glass transition points (T_g) of the Bi-Zn-B glass follow a decreasing trend with the Bi_2O_3 ratio between 460 and 354 °C (Fig. 1 d) as Bi_2O_3 can break the B-O bond as denoted by previous research [39]. However, an increase in the Bi concentration can simultaneously reduce chemical durability and waste loading. In this study, 30 wt% of Bi_2O_3 with a glass transition temperature of approximately 405 °C was selected to act as the matrix material for the waste form to compromise the waste loading, chemical durability, and the glassfication point as denoted in the Supplemental Fig. S2.

The as-synthesized $Cs_2NaInCl_6$ exhibited high purity without a secondary crystalline phase, as shown in the XRD profile in Fig. 1e. The corresponding on-set decomposition point of the perovskite was at approximately 604 °C, as denoted in the TGA-DSC curves; the second weight loss step at approximately 620 °C can be attributed to the evaporation of Cs and Cl, which is consistent with previous studies (Fig. 1f) [11]. The Tg-Tx interval can be identified as the processing interval for the glass-ceramic composite, and 430 °C lies within this glass-ceramic processing range (Fig. 1d). Therefore, the current hot-pressing technique can successfully consolidate the composite waste form without elemental evaporation or loss as the glassification point of the Bi-Zn-B glass is approximately 430 °C.

The perovskite XRD peak intensity increased with increasing composition of the composite waste form, as shown in Fig. 2a and b, which is evidenced by semi-quantitative analysis (the detail of the Rietveld peak refinement of XRD patterns is shown in Fig. S3) wherein the $Cs_2NaInCl_6$/glass ratio shifts from 4.4/1 to 1/1.8 when the $Cs_2NaInCl_6$ ratio increases from 30 wt% to 70 wt%. The intensity of the characteristic Raman for $Cs_2NaInCl_6$ $2A_{1g}$ (293 cm^{-1}) also increases, along with BiOCl A_{1g} (144 cm^{-1}), with an increasing $Cs_2NaInCl_6$ ratio (Fig. 2c). A continuous decrease in peak intensity was observed at approximately 410 cm^{-1}, which is associated with the vibrations of the BiO_6 octahedral structure within the Bi-Zn-B glass [27], which can be attributed to the gradual formation of BiOCl.

The composite waste form with $Cs_2NaInCl_6$ composition of 30–70 wt % featured high theoretical density and dual-phase structure, as

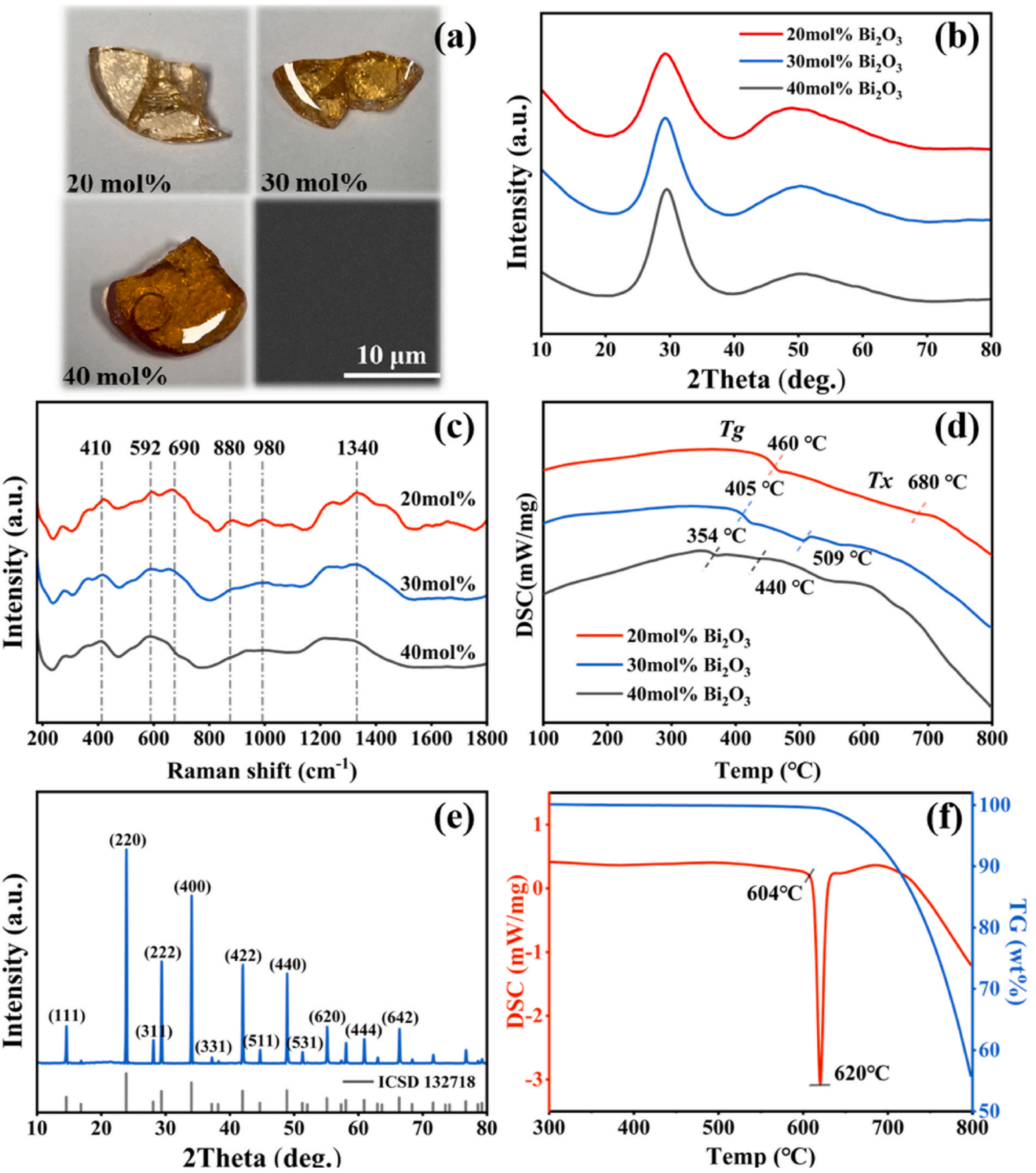

Fig. 1. (a) Photographs and surface morphology of Bi-Zn-B glass with varying bismuth oxide (Bi_2O_3) contents. (b) XRD patterns of Bi-Zn-B glass. (c) Raman spectroscopy analysis of Bi-Zn-B glass. (d) TGA-DSC curve of the Bi-Zn-B glass. (e) XRD patterns of $Cs_2NaInCl_6$ perovskite. (f) TGA-DSC curve of $Cs_2NaInCl_6$ perovskite.

evidenced by the SEM image in Fig. 2e. The Vickers hardness of the composite is presented in Fig. S4, where the sample with 50 wt% perovskite content exhibits a Vickers hardness of up to 726 HV. The composite waste form morphology transitions from a dense glassy phase to more intertwined multiphase connectivity, and ultimately resulting in a structure with a predominant dark perovskite phase when the $Cs_2NaInCl_6$ content increases and the corresponding measured density from 4.24 g/cm^3 to 3.63 g/cm^3 and theoretical density from 95.5 % to 98.1 %, respectively (Fig. 2d).When perovskite addition exceeds 50 wt %, non-uniform grain growth occurs on the surface of the multiphase solidified sample which indicates the perovskite content has surpassed the glass matrix's accommodation threshold, preventing complete encapsulation.

3.2. *Microstructural evolution of the composite after semi-dynamic leaching experiments*

The chemical durability and microstructural evolution of the composite waste (50 wt% perovskite) was further evaluated through the 28-d semi-dynamic leaching test at RT and 90 °C (Figs. 3 and 4). After leaching, the composite waste retained its original multiphase structure; however, the perovskite phase on the composite waste surface

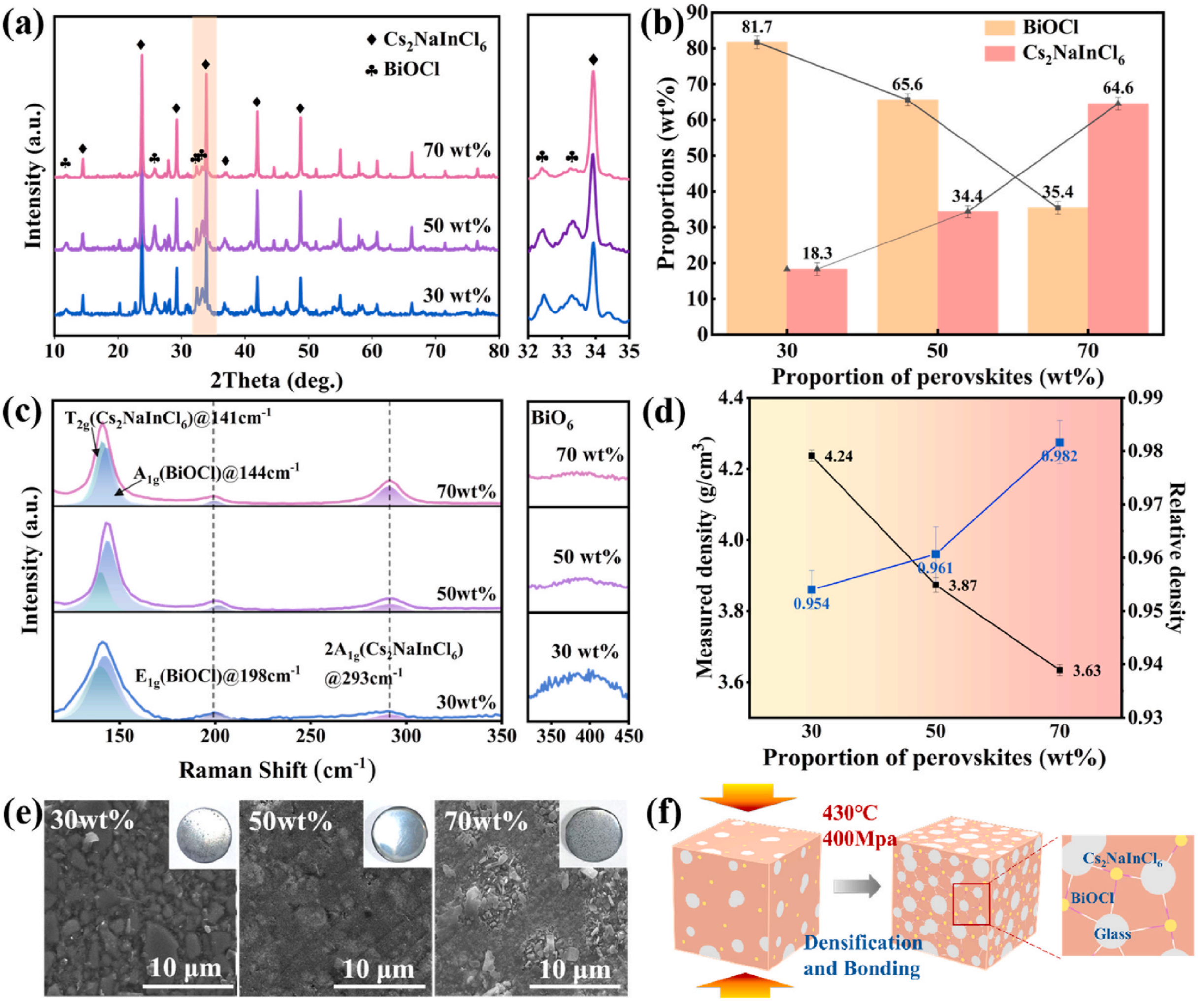

Fig. 2. (a) XRD patterns of the composite waste form with different amounts of $Cs_2NaInCl_6$. (b) Proportion of $Cs_2NaInCl_6$ in the composite waste form derived from XRD peak refinement. (c) Raman peaks of the composite waste form with varying $Cs_2NaInCl_6$ content. (d) Measured density and theoretical density with different amounts of $Cs_2NaInCl_6$. (e)Variations in surface morphology of composite waste form with different amounts of $Cs_2NaInCl_6$. (f) Schematic diagram of the composite waste form fabrication process.

underwent phase degradation and reorganization during the leaching experiment, leaving behind nanoscale microspherical corrosion products with Bi, In, Cl, and O enrichment on the sample surface at RT (Fig. 3a and b and c). The surface corrosion can further be accelerated at an elevated temperature of 90 °C, resulting in cubic In_2O_3 grains and flake-like BiOCl structures growing in the corrosion voids between phases forming on the waste form surface (Fig. 3d and e) [40]. Moreover, the small and dense microspheres, denoted by the peak broadening and redshift of the wavelengths in the Raman spectra, were accelerated by the reaction between the sample and water.

Fig. 4a shows the XRD patterns of the composite waste form before and after leaching at RT and 90 °C. The BiOCl and $Cs_2NaInCl_6$ chalcogenide phases of the original samples were significantly degraded by 28 d of RT water corrosion, and the intensity of the relevant diffraction peaks decreased or even disappeared, while the relevant diffraction belonging to the structure of In_2O_3 was detected on the surface of the sample under the accelerated leaching test at 90 °C. The Raman vibrational peaks around ~141 cm^{-1} and ~293 cm^{-1} represent the T_{2g} (mainly associated with $[InCl_6]$ octahedral bending vibrations) and $2A_{1g}$ ($[InCl_6]$ octahedral symmetric stretching vibrations) modes of the original $Cs_2NaInCl_6$ double perovskite (Fig. 4b) [41,42]. Meanwhile, the peak positions around 59, 144, and 198 cm^{-1}, corresponding to the A_{1g} (Bi-Cl external stretching vibration) mode, A_{1g} (internal Bi-Cl stretching vibration) mode, and E_{1g} (internal Bi-Cl stretching vibration) mode of the BiOCl structure, exhibited a decrease in the intensity of the BiOCl vibrational peaks, along with broadening and a shift towards higher wavenumbers, which can be attributed to the surface amorphization and grain subdivision during the leaching process [27,43]. In addition, the corrosion also induced the growth of In_2O_3, as evidenced by the Raman peak positions around 96 cm^{-1} and 308 cm^{-1} [44].

Furthermore, a significant weakening of the Cs 3d peak ($Cs3d_{5/2}$:724.0 eV, $Cs3d_{3/2}$:738.0 eV) and a shifting of the Bi 4f peak from 158.7 eV to a higher binding energy (158.9 eV) occur after leaching, suggesting a change in the coordination environment of Bi^{3+} as denoted by the XPS (Fig. 4c and d) [45]. During leaching, Cs on the sample surface readily dissolves in water, leaving a Cs-leaned surface alteration layer, resulting in the absence of a Cs signal. Meanwhile, Bi in Bi_2O_3 recombines with Cl to form the BiOCl structure, while the OCl^{3-} group, which has higher electronegativity than O^{2-}, exerts a stronger attraction to electrons, thereby increasing the binding energy of Bi^{3+}. As shown in Fig. 3f, the Cl 2p peak initially consisted of two groups from $Cs_2NaInCl_6$ ($Cl2p_{3/2}$:198.5 eV, $Cl2p_{1/2}$:200.2 eV) and BiOCl ($Cl2p_{3/2}$:197.5 eV, $Cl2p_{1/2}$:199.2 eV), differing by 1.0 eV. The intensity of the Cl 2p peak related to $Cs_2NaInCl_6$ sharply decreased in the RT leaching test, while the peaks around 197.5 eV and 199.2 eV associated with the BiOCl structure were successfully retained post the 90 °C leaching test, suggesting the robust water resistance of BiOCl [45,46]. Regarding In 3d shown in Fig. 3e, the binding energy of the samples decreased by 0.3 eV

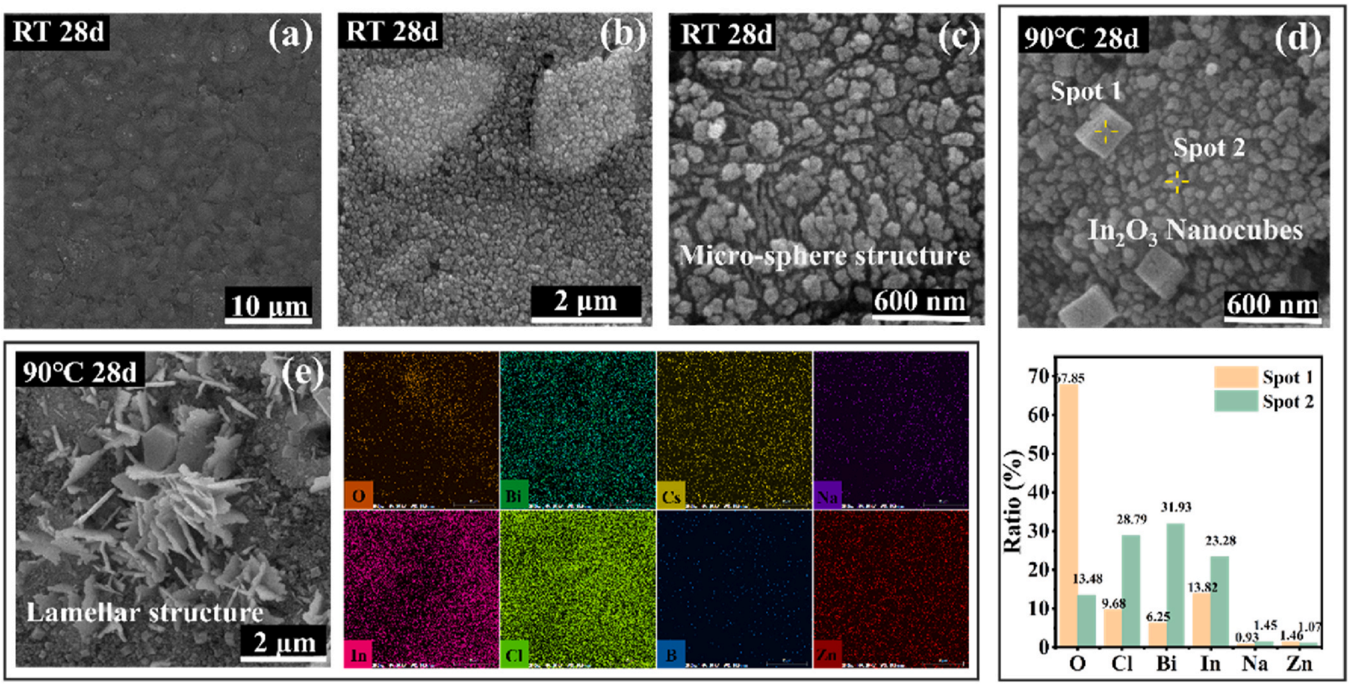

Fig. 3. Surface morphology of the composite waste form after semi-dynamic leaching tests: (a) (b) and (c) illustrate the surface morphology of the composite waste form after room temperature (RT) leaching test. (d)(e) Cubic and microspherical corrosion products on the sample surface after leaching at 90 °C for 28 d, along with EDS analysis.

after leaching, indicating the transformation from $Cs_2NaInCl_6$ ($In3d_{5/2}$:452.3 eV, $In3d_{3/2}$:444.7 eV) to In2O3($In3d_{5/2}$:452.0 eV, $In3d_{3/2}$:444.4 eV) [47,48]. In addition, asymmetric peaks of $In(OH)_3$ [49] were observed for the sample after the RT leaching test, suggesting an intermediate state during the phase degradation of $Cs_2NaInCl_6$ to In_2O_3.

In-situ Raman spectroscopy experiments with a timeframe of 424 h were performed on the composite waste form with 50 wt% of perovskite to explore the time-dependent simultaneously microstructural and chemical evolution of the composite waste form in contact with water. As denoted in Fig. 5a, the laser beam was focused on the solid/liquid interface with a testing zone of around 16 μm on either side of the solid–water interface. As illustrated in Fig. 5b, the characteristic peaks associated with the BiOCl structure at 59, 144, and 198 cm^{-1} remain unchanged, whereas the $2A_{1g}$ vibration peak related to $Cs_2NaInCl_6$ at 293 cm^{-1} weakens within the first 4 h, indicating the rapid dissolution of $Cs_2NaInCl_6$ during the early leaching regime, corresponding to the significantly higher elemental release rate observed on the first day (Fig. 7a). The corrosion product of In_2O_3 gradually emerges on the sample surface after 96 h, correlating with the transition point in the leaching curve (Fig. 7a), where the leaching rate shifts from rapid to slow, indicating a dominance of diffusion over dissolution processes.

Changes in the solid–water interface were observed over 424 h using in-situ Raman spectroscopy are shown in Fig. 5c, and the corrosion interface displacement and corresponding fitted displacement rate curves are shown in Fig. 5d and f. The displacement curves for the perovskite characteristic peak (141 cm^{-1}) and water peak (3400 cm^{-1}) follow a lognominal descending trend, indicating the mechanism changes from matrix dissolution to diffusion that occurred on day-5, which is consistent with the leaching rate curves in the following section. The initial position of the solid–liquid interface corresponds to the 2 μm mark on the coordinate axis, with a rapid decrease in displacement speed during the initial leaching stage (Fig. 5e and g show the fitted curves). Post 96 h, the solid–liquid interface exhibits minimal movement, with the matrix retracting approximately 4 μm. Moreover, the perovskite matrix simultaneously undergoes retraction with the forward movement of the Raman peak of the water molecule, confirming that the surface alteration layer was hydrolyzed. In addition, the corrosion product In_2O_3 was detected at 96 h, which is consistent with the previous XRD profile, suggesting that gradual phase degradation and structural reorganization occurred.

3.3. *MD simulation of the perovskite/water interaction*

To further investigate the interaction mechanisms between perovskite and water, as well as the behavior of the corresponding elements in solution, molecular dynamics (MD) simulations were conducted under an NVT ensemble at 350 K, which is higher than the leaching-experiment temperature used in this study to accelerate the corrosion behavior within the picosecond simulation range. Based on the XRD pattern of the perovskite shown in Fig. 1a, three low-index crystallographic directions of $Cs_2NaInCl_6$ [(100), (110), and (111)] were considered to study the release characteristics of different elements along these directions. According to Bravais' law [50], planes have low surface energies, making them likely to be exposed during crystal growth, as confirmed by the XRD measurements. Initial and final snapshots of the MD simulations along these three crystallographic directions are shown in Fig. 6a and b and supplemental Videos S1–S3. The results indicate that within the 6–10 ps simulation time, Na, Cl, and Cs atoms near the surface diffused significantly into the H_2O region and interacted strongly with H_2O molecules, causing the collapse of the surface crystal structure. Because of the lighter masses of Cl and Na, these elements easily escape from the matrix and diffuse into the water. In Fig. 6c, a steeper slope of the MSD curves corresponds to a faster release rate of the elements. Na readily escapes from the (100) plane of $Cs_2NaInCl_6$, whereas Cs diffuses rapidly from the (111) plane. Cl exhibits significant release rates in both the (110) and (111) directions. In contrast, the release rate of In is considerably lower than those of the other three elements, indicating that the chemical stability of $Cs_2NaInCl_6$ exhibits strong anisotropy.

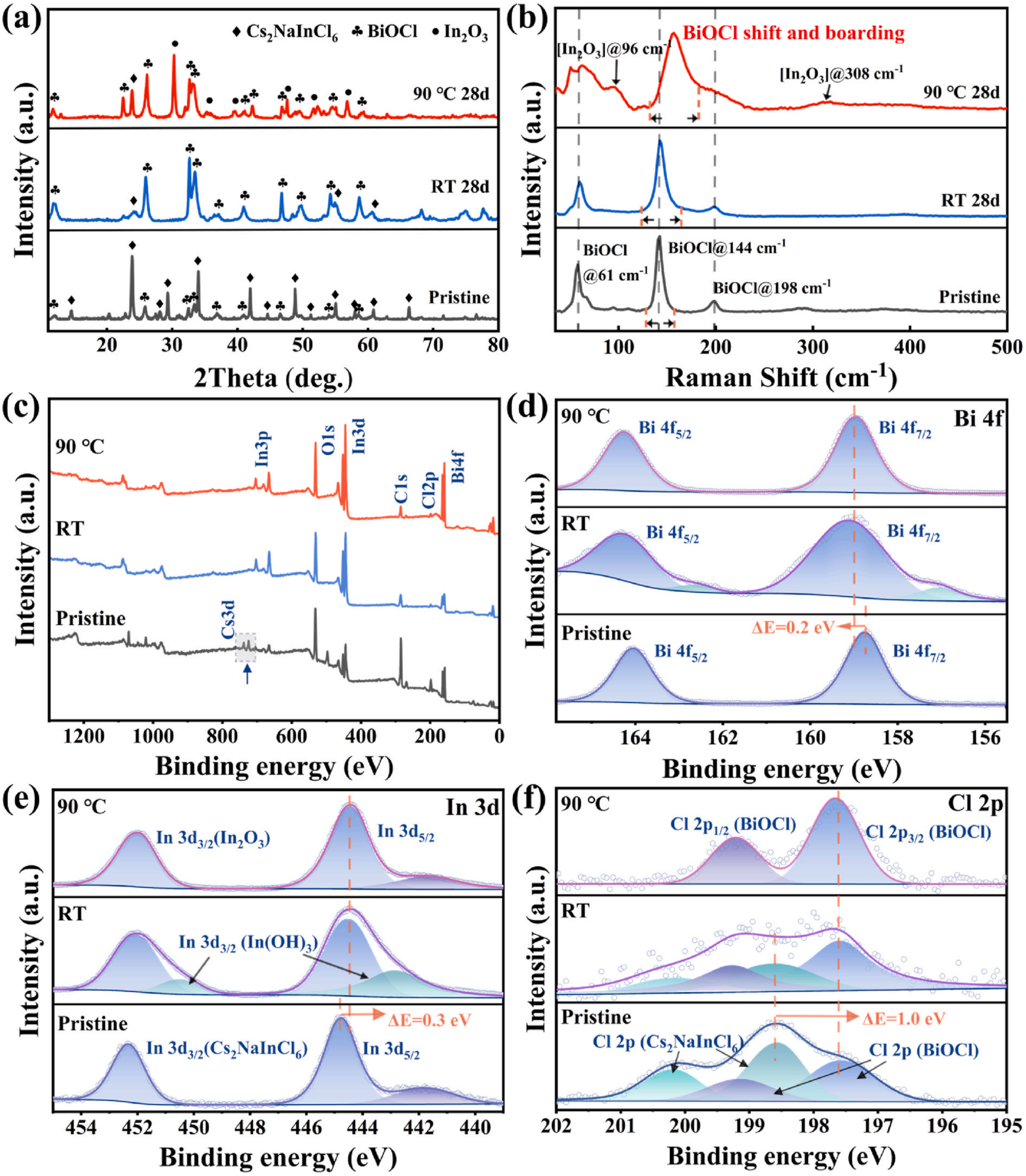

Fig. 4. (a) XRD patterns of the samples before and after the leaching test. (b) Raman spectra of the samples before and after the leaching test. (c) Total XPS spectra of the samples before and after the leaching test. (d) XPS Bi4f spectra. (e) XPS In3d spectra. (f) XPS Cl2p spectra.

3.4. *Chemical durability and leaching mechanism of composite*

The leaching rates of the key elements in the composite waste form exhibited a lognominal decreasing trend, as shown in Fig. 7a and b. All elements exhibited a high initial leaching rate during the early stage of the leaching experiment (0–5 d), followed by a gradual decline (dissolution stage), and finally changed to the diffusion stage with a corresponding slow elemental release rate, consistent with the in-situ Raman curves. The elemental leaching is thermodynamically driven because the mechanism changes from dissolution to diffusion was accelerated at 90 °C (Fig. 7). The cumulative concentrations of Cs, Na, In, Cl, Bi, and Zn in the leachate are presented in Supplementary Fig. S5 and were fitted using the Cote model [31], with the relevant fitting parameters detailed in Table S1. The normalized long-term leaching rates derived from the k_1 values of the Cote model fitting curves are summarized in Table S2. Notably, Cl in the perovskite composition exhibited the highest long-term release rate, followed by Na and Cs, whereas In exhibited the lowest release rate. In addition, the release rate of Bi was significantly lower than that of Zn in the glass matrix owing to its low solubility and the passivating effect of BiOCl on Bi. Fig. 7c and d illustrate the atomic ratios of Cs/Cl and Zn/Bi, respectively, with a rapid exchange between the incongruent and congruent leaching mechanisms. The released amounts of Cs and Cl greatly exceeded one-third of the stoichiometric ratio in the early stage because partial of the BiOCl had already been

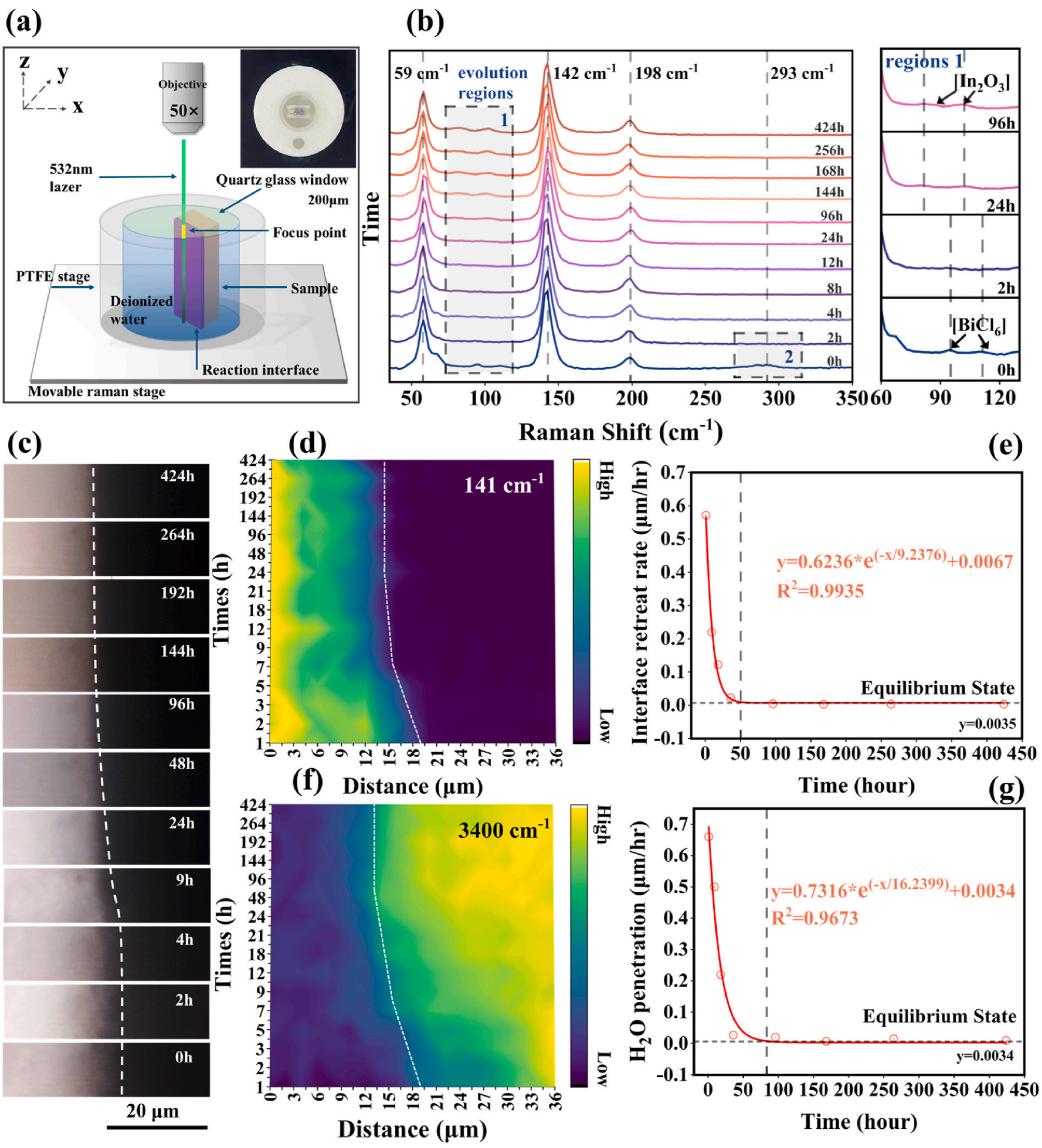

Fig. 5. (a) Schematic of the in-situ Raman testing platform. (b) Raman peaks associated with BiOCl and $Cs_2NaInCl_6$ at the interface of waste form/water over a testing duration of 424 h. (c) Optical images of interface morphology evolution of the composite waste form during a leaching period of 424 h. (d) Changes at 141 cm^{-1} at the interface between the waste form and water. (e) Retraction rate of the boundary of waste form at 141 cm^{-1} at the interface along with the corresponding fitting equation. (f) Changes of the water peak at 3400 cm^{-1} at the interface between the waste form and water. (g) Forward rate of water peak at 3400 cm^{-1} at the interface along with the corresponding fitting equation.

formed during the sample sintering. However, as the time approached 5 days, the release rate of Cl started to exceed that of Cs. This can be attributed to the continuous formation of BiOCl during the leaching process, which affects their leaching behaviors. The leaching rate of Bi in the glass is significantly lower than that of Zn, which can be attributed to the inherent stability of Bi and the protective effect of the BiOCl passivation structure.

4. Discussion

4.1. Low-temperature consolidation of the halide waste stream

Generally, the BiOX passivation structure is generated through a diffusion-reorganization process, where the Bi and halide elements in the waste form first dissolve and saturate in an aqueous solution, followed by reprecipitation on the surface to form an insoluble BiOX structure, which can deter elemental release [10]. Herein, a water-resistant BiOCl structure was introduced into the matrix during the low-temperature, high-pressure consolidation of the composite

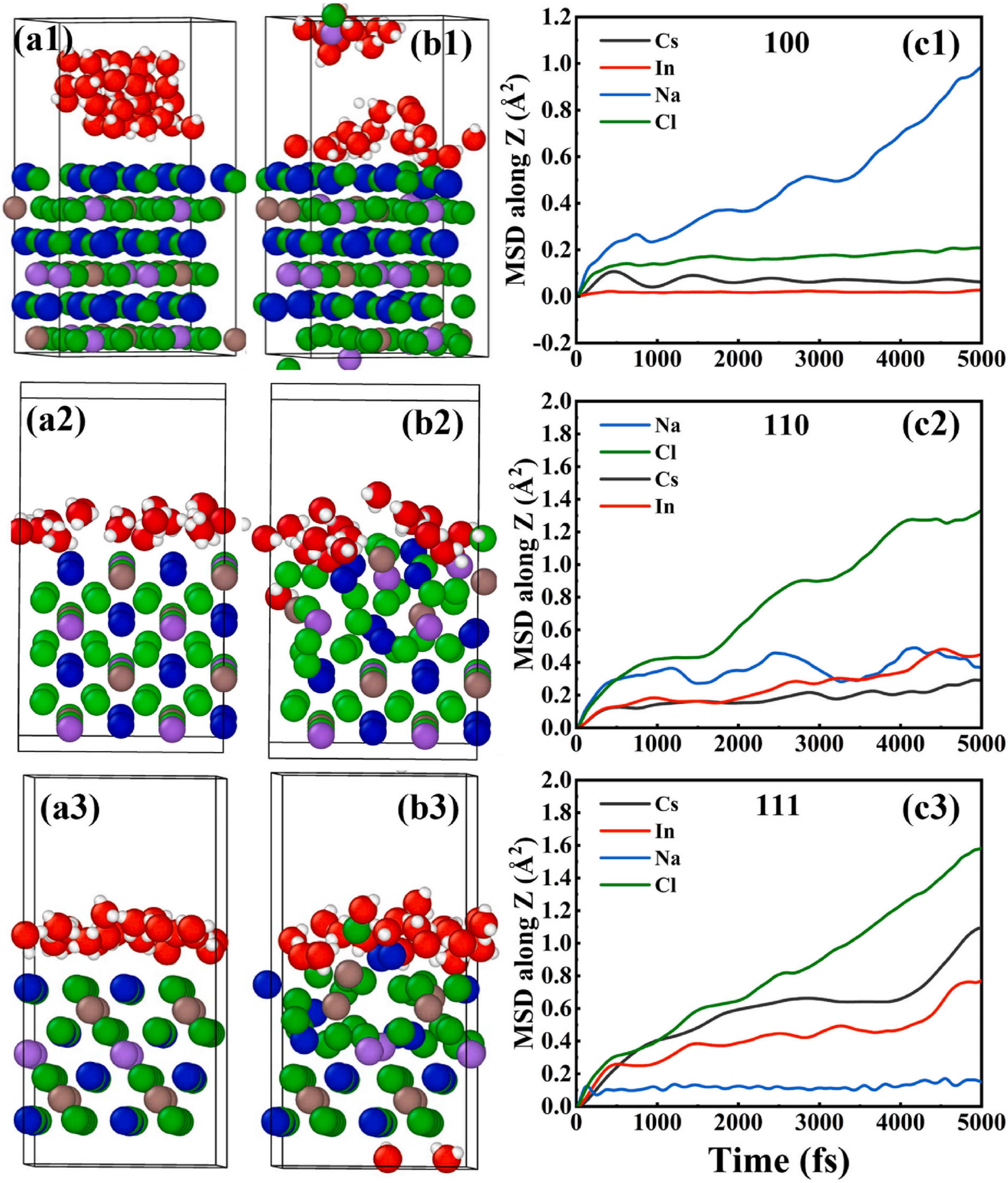

Fig. 6. Initial snapshot (a1-a3) and final snapshot (b1-b3) of the ab initio molecular dynamic simulations and average mean squared displacement (c1-c3) of the unfixed atoms near the surface along the z direction of the $Cs_2NaInCl_6$ (100), (110) and (111) crystallographic directions when in contact with H_2O at 350 K. The red, white, blue, green, brown, and violet spheres represent O, H, Cs, Cl, In, and Na atoms, respectively. The MD simulation lasted 10 ps, 6 ps, and 6 ps for $Cs_2NaInCl_6$ (100), (110), and (111), respectively.

waste form, increasing the structural reliability of the perovskite component within the stable Bi-Zn-B glass matrix by delaying water penetration (Fig. 2f). As the perovskite content increases, the Bi elements within the octahedra bond with $Cs_2NaInCl_6$ to form BiOCl, leading to a continuous decrease in the intensity of the peak at ~380 cm^{-1} (BiO_6 octahedron). At 50 wt% perovskite addition, the vibrational peak corresponding to the BiO_6 octahedral structure nearly disappears (Fig. 2c), indicating that there are no excess BiO_6 octahedral units available for bonding with $Cs_2NaInCl_6$, thereby demonstrating that the maximum encapsulation efficiency has been reached at this perovskite content. When the perovskite content reaches 70 wt%, numerous defects appear on the surface of the composite waste form, indicating that the glass encapsulation capacity for the perovskite has reached its limit, the Bi-Zn-B glass is no longer able to form sufficient BiOCl structures to effectively immobilize the perovskite phase. Therefore, considering the curing efficiency and structural integrity, 50 wt% $Cs_2NaInCl_6$ was added for subsequent experiments.

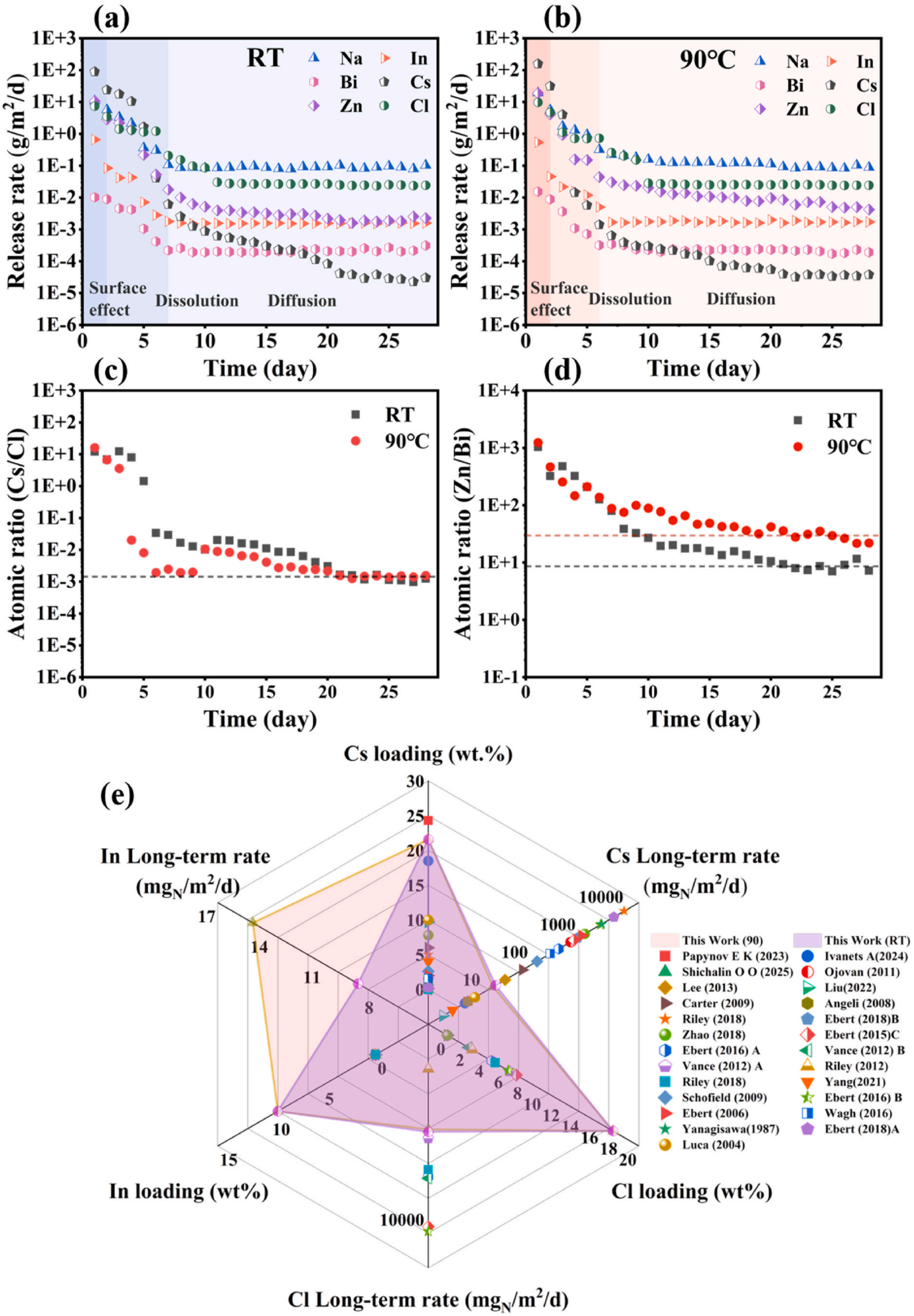

Fig. 7. (a) and (b) Illustration of the elemental release rates of Cs, Na, In, Cl, Bi, and Zn from the composite waste form during semi-dynamic leaching tests conducted in deionized water at RT and 90 °C. (c) and (d) Atomic ratios of Cl/Cs and Zn/Bi, respectively, observed in the same semi-dynamic leaching experiment at both temperatures. (e) Comparison of the waste-loading capacity and chemical durability of the composite waste form in this study with those reported in the literature.

4.2. Mechanisms of aqueous corrosion evolution in composite waste form

The microstructural evolution and phase degradation of the composite waste form are not intrinsic and are highly dependent on its surface alteration behavior [51]. In the current study, a dissolution–reorganization mechanism dominated the microstructural evolution of the composite waste form, as confirmed by the SEM, XPS, and Raman spectra (Figs. 3–5). Specifically, as illustrated in Fig. 8, the water diffuses through the composite dual-phase interface and reacts with $Cs_2NaInCl_6$, inducing the dissolution of partial $Cs_2NaInCl_6$ into a two-dimensional layered structure, with Cs atoms occupying the hexagonal channels between $[NaInCl_6]^{2-}$ octahedra due to van der Waals forces [52]. The Raman spectra of $Cs_2NaInCl_6$ indicate that water molecules induce chemical bonding breakage, exposing $InCl_3$ octahedra and leading to phase degradation to CsCl and NaCl, as shown in Equation (5). Over time, In_2O_3 structures are formed through the hydration–dehydration of $InCl_3$, and BiOCl arises from the reorganization of enriched elements on the composite surface, covering the dissolution defects of the perovskite, passivating the surface, and preventing further reaction with water (Equations (6)–(8)).

The weak van der Waals forces between the two-dimensional layered structures were easily disrupted, resulting in the rapid release of Cs and Cl in the early phase, as demonstrated by the MD simulations and supplementary Videos S1–S3. Given the larger ionic size of Cs, the binding strength between Cs and Cl is weaker than that between Na and Cl, or In and Cl, resulting in the highest release rate for Cs. The passivating structures of In_2O_3 and BiOCl covered the surface of the sample, leading to a transformation of the leaching mechanism from dissolution to diffusion. Notably, the formation of In_2O_3 precipitate was observed on the surface of the sample under 90 °C (Fig. 3d), and its diffraction peaks were also identified in the XRD pattern (Fig. 4a). This suggests that the low leaching rate of In can be attributed to its potential precipitation as In_2O_3, which leads to a reduction in elemental diffusion.

$$Cs_2NaInCl_6 \rightarrow 2CsCl + NaCl + InCl_3 \tag{5}$$

$$InCl_3 + 3H_2O \rightarrow In(OH)_3 + 3HCl \tag{6}$$

$$2In(OH)_3 \rightarrow In_2O_3 + 3H_2O \tag{7}$$

$$BiCl_3 + H_2O \rightarrow BiOCl + 2HCl \tag{8}$$

In the current study, a dissolution–diffusion leaching mechanism dominated the elemental release of the composite waste form, with the elemental release mechanism shifting from incongruent to congruent and finally to incongruent, as shown in Fig. 7. The initial dissolution behavior of the perovskite can be revealed by MD simulations, where the electrostatic interactions lead H^+ to be preferentially associated with the negatively charged Cl^-, while O^{2-} tends to bond with the positively charged Na^+ and Cs^+ ions (Fig. 6), strengthening the interactions between CsCl, NaCl, and H_2O. The elemental leaching behaviors simulated in the MD studies within the picosecond range aligned well with the initial stage of the leaching behavior without the formation of a passivation film, where the rapid release of Cs, Cl, and Na was observed. It is noteworthy that the normalized long-term leaching rate of samples immersed at 90 °C is lower than that of samples immersed at RT. This phenomenon can be attributed to the more vigorous exchange between substances at 90 °C, which accelerates the surface diffusion–reorganization processes, leading to the rapid formation of BiOCl passivation film. Although the elemental leaching rate increased in the early stages at 90 °C, the corresponding acceleration of the reorganization process resulted in the formation of surface passivating structures. These structures subsequently hinder the material exchange between water and the matrix by triggering a mechanism shift to diffusion, thereby reducing the long-term leaching rate.

Overall, the leaching behavior of the composite waste form is schematically discussed in the following Fig. 8. The initial interaction between the waste form and water molecules leads to a fast elemental release, which can be attributed to its intrinsic structural stability, as denoted in the MD simulation. The anisotropic properties of the waste form resulted in the fast release of compositional elements, with the release rate decreasing from Cs to In, according to the MSD analysis (Fig. 6). The fast release of Bi, Cl, and In then results in the localized saturation of the elements, gradually forming insoluble BiOCl, In_2O_3, and amorphous passivating layers during the subsequent leaching processes. Consequently, the leaching mechanism of the composite waste shifts from dissolution to matrix diffusion, with a rapid reduction in the elemental release rate. The continuous accumulation of Cl, In, and Bi elements at the solid/liquid interface leads to reorganization processes

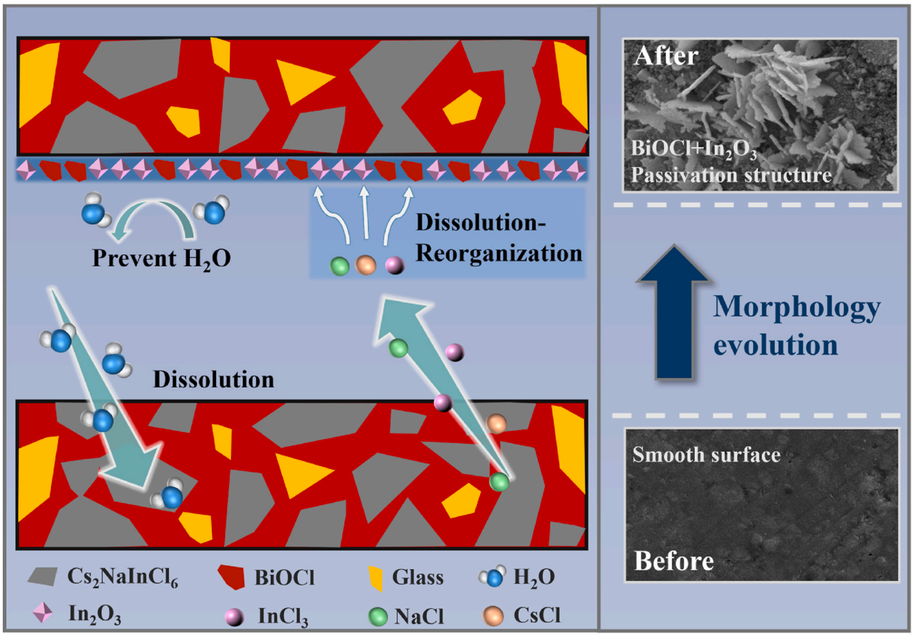

Fig. 8. Schematic demonstrating the water induced microstructure evolution of the waste form.

that facilitate the growth of water-resistant BiOCl or In_2O_3 structures at the defects, which protect the susceptible $Cs_2NaInCl_6$ from water corrosion. Consequently, owing to the increased limitations on transport between the solution and sample, the dissolution of the composite waste form ceased effectively.

4.3. Comparison between composite waste form and advanced solidification methods

The waste-loading capacity and chemical durability of the composite waste form were compared with existing literature[53–73], with the results summarized in Table S3 and visualized in Fig. 7e, the developed composite waste form with 50 wt% $Cs_2NaInCl_6$ demonstrates encapsulation rates of 21.6 wt% and 17.3 wt% for Cs and Cl, respectively, significantly exceeding the state-of-art halide waste form. In addition, the currently developed waste form can further immobilize Na or K, which are the main components of the eutectic salt, and high-valence state radionuclides, namely In, Nd, La, Ce, and Y, as fission elements with a corresponding immobilization ratio of 1.8 wt% for Na, and 9.3 wt % for In, separately. The normalized long-term leaching rates for Cs, Na, In, and Cl under RT conditions are 0.019, 0.041, 0.009, and 0.057 $g_N/m^2/d$, respectively; whereas under 90 °C conditions, the normalized long-term leaching rates are 0.017, 0.019, 0.015, and 0.049 $g_N/m^2/d$, respectively, reflecting superior performance compared to analogous materials.

Therefore, the advanced waste form based on halide double perovskites, shown in Fig. 7e, presents substantial advantages as an environmentally friendly waste form capable of simultaneously immobilizing Cs, In, and Cl with enhanced chemical durability and high waste-loading capacity. Moreover, the highly tunable crystalline structure of the current waste form (Cs_2ABX_6, A = K, Na; B=In, Nd, La, Ce; X = F, Cl, Br, I) provides a feasible way to immobilize these radionuclides in MSRs by substituting the chemical composition of the current crystalline structure to generate a novel waste form, which can significantly broaden their application in waste separation and accommodation. Importantly, the composite waste form exhibits low-temperature curing capabilities that surpass those of other waste forms, along with the potential selective separation of molten salt elements, making it a highly viable option for effectively managing complex and easily migratory wastes from MSRs.

The author further explored the pressureless and low-temperature (600 °C) sintering process for the composite waste form to facilitate its industrial application through coupling melting of the perovskite (15–25 wt%) with the waste form as denoted in Supplemental Fig. S6. The as-fabricated waste form demonstrated a uniform elemental distribution and smooth sample surface, with a measured theoretical density above 95 %. However, further research is required to fundamentally understand the microstructural evolution and phase degradation behavior of the current waste form, which could provide the necessary guidelines for the design and fabrication of robust protective matrices to simultaneously enhance the chemical durability and waste loading of double perovskites.

5. Summary and conclusions

This study demonstrated a novel strategy to simultaneously immobilize halide radionuclides, Cs, and eutectic salt elements through a low-temperature process. A self-assembled Bi-Zn-B low-temperature glass was successfully fabricated with a glassification point of approximately 400 °C. This approach enables a high encapsulation capacity for the elements from salt waste streams (Cs, In, and Cl) while achieving excellent chemical durability. The key findings are summarized as follows.

1. Multiple radionuclide elements from the MSRs salt waste stream can be simultaneously immobilized into the glass matrix at a temperature as low as 430 °C, demonstrating a high waste-loading capacity (the waste loading of Cs, In, and Cl are 21.6, 9.3, and 17.3 wt%, respectively) and outstanding chemical durability (the normalized long-term leaching rates for Cs, In, and Cl are 0.017, 0.015, and 0.049 $g_N/m^2/d$, respectively, under 90 °C).
2. The thermodynamically driven diffusion of water molecules and surface reconstruction occurs within the alteration layer of the sample surface. Initial rapid dissolution was followed by the release of Cs, Na, In, and Cl, which underwent prolonged diffusion. Additionally, the gradual reprecipitation of Bi, Cl, and In occurred in the alteration layer.
3. During the initial phase, an incongruent leaching mechanism predominates the release of elements from the composite waste form, which is primarily determined by the bond strength within the 2D structure of the double perovskite. Moreover, the BiOCl passivation structure formed between the micro-sized bismuth zinc borate glass matrix and $Cs_2NaInCl_6$ aided in stabilizing the corrosion-sensitive $Cs_2NaInCl_6$ component.
4. The chemical stability of the chemical components (Cs, Na, In, and Cl) within the double perovskite structure exhibited anisotropic characteristics, manifesting as favorable elemental release of Cs and Cl along the (111) crystallographic direction and Na and Cl along the (100) and (110) directions, respectively. Notably, indium demonstrated the highest structural stability, which is consistent with experimental observations.

Overall, this study demonstrates the feasibility of employing halide double perovskites as a potential waste form capable of effectively immobilizing salt waste streams from advanced nuclear energy systems such as MSRs or the electropyroprocessing of spent nuclear fuel.

CRediT authorship contribution statement

Hao Ji: Writing – original draft, Visualization, Validation, Investigation. **Kun Yang:** Writing – review & editing. **Wangwei Ru:** Software. **Yibo Wang:** Software. **Ke Yang:** Software. **Feida Chen:** Supervision. **Chengying Bai:** Supervision. **Xiaobin Tang:** Supervision.

Declaration of competing interest

The authors declare that they have no known competing financial interests or personal relationships that could have appeared to influence the work reported in this paper.

Acknowledgement

The authors would like to express appreciation for financial support from Natural Science Foundation of Jiangsu Province (BK20230898); National Natural Science Foundation of China (No. 37244600).

Appendix A. Supplementary data

Supplementary data to this article can be found online at https://doi.org/10.1016/j.ceramint.2025.09.024.

References

[1] A.Y. Galashev, Processing of fast neutron reactor fuel by electrorefining: thematic overview, Int. J. Energy Res. 45 (2021) 11459–11478, https://doi.org/10.1002/er.6267.

[2] B.J. Riley, W.C. Lepry, J.V. Crum, Solution-derived sodalite made with Si- and Ge-ethoxide precursors for immobilizing electrorefiner salt, J. Nucl. Mater. 468 (2016) 140–146, https://doi.org/10.1016/j.jnucmat.2015.11.011.

[3] B.J. Riley, J.D. Vienna, S.M. Frank, J.O. Kroll, J.V. Peterson, N.L. Canfield, Z. Zhu, J. Zhang, K. Kruska, D.K. Schreiber, J.V. Crum, Glass binder development for a glass-bonded sodalite ceramic waste form, J. Nucl. Mater. 489 (2017) 42–63, https://doi.org/10.1016/j.jnucmat.2017.03.041.

[4] E.Y. Choi, S.M. Jeong, Electrochemical processing of spent nuclear fuels: an overview of oxide reduction in pyroprocessing technology, Prog. Nat. Sci. Mater. Int. 25 (2015) 2–582, https://doi.org/10.1016/j.pnsc.2015.11.001.

[5] J.P. Ackerman, T.R. Johnson, L.S.H. Chow, E.L. Carls, W.H. Hannum, J.J. Laidler, Treatment of wastes in the IFR fuel cycle, Prog. Nucl. Energy 31 (1–2) (1997) 141–154, https://doi.org/10.1016/0149-1970(96)00008-X.

[6] M.I. Ojovan, J.M. Juoi, W.E. Lee, Application of glass composite materials for nuclear waste immobilization, J. Pak. Mater. Soc 2 (2) (2008) 72–76.

[7] D. Leng, X. Li, Y. Lv, et al., Comprehending the stability of Sr2+ immobilization in chemically bonded phosphate ceramic system: a mechanism study, Ceram. Int. 48 (7) (2022) 10209–10219, https://doi.org/10.1016/j.ceramint.2021.12.234.

[8] D. Leng, X. Li, Y. Lv, et al., Cesium immobilization by K-struvite crystal in aqueous solution: ab initio calculations and experiments, J. Hazard Mater. 387 (2020) 121872, https://doi.org/10.1016/j.jhazmat.2019.121872.

[9] R.A.H. El-Mallawany, Tellurite Glasses Handbook: Physical Properties and Data, CRC Press, Boca Raton, 2001, https://doi.org/10.1201/9781420042085.

[10] K. Yang, W. Zhu, S. Scott, Y. Wang, B.J. Riley, J. Vienna, J. Lian, Immobilization of cesium and iodine into Cs3Bi2I9 perovskite-silica composites and core-shell waste forms with high waste loadings and chemical durability, J. Hazard Mater. 401 (2020) 123279, https://doi.org/10.1016/j.jhazmat.2020.123279.

[11] S.M. Scott, W. Zhu, T. Yao, R.C. Vienna, R.C. Ewing, J. Lian, The thermal stability and consolidation of perovskite variant Cs$_2$SnCl$_6$ using spark plasma sintering, J. Am. Ceram. Soc. 101 (2018) 2060–2065, https://doi.org/10.1111/jace.15372.

[12] D. Han, K. Yang, C. Bai, F. Chen, Y. Sun, Y. Wang, H. Ji, Z. Yang, X. Tang, Thermal and chemical durability of metal halide perovskite CsPbBr3 single crystals, Chem. Eng. J. 475 (2023) 146209, https://doi.org/10.1016/j.cej.2023.146209.

[13] T. Leijtens, G.E. Eperon, N.K. Noel, S.N. Habisreutinger, A. Petrozza, H.J. Snaith, Stability of metal halide perovskite solar cells, Adv. Energy Mater. 5 (2015) 1500963, https://doi.org/10.1002/aenm.201500963.

[14] K. Yang, Y. Wang, J. Shen, S.M. Scott, B.J. Riley, J.D. Vienna, J. Lian, Cs3Bi2I9-hydroxyapatite composite waste forms for cesium and iodine immobilization, J. Adv. Ceram. 11 (2022) 712–728, https://doi.org/10.1007/s40145-021-0565-z.

[15] Q. Sun, W. Yang, Y. Liu, Y. Li, M. Li, Microstructure and mechanical properties of tempered glass joint bonded with Bi-B-Zn low melting glass, J. Mater. Process. Technol. 271 (2019) 404–412, https://doi.org/10.1016/j.jmatprotec.2019.02.017.

[16] J. Chen, Y. Li, W. Miao, C. Mai, M. Li, Bonding Cu to Al2O3 with Bi-B-Zn oxide glass via oxidation–reduction reaction, J. Electron. Mater. 47 (2018) 542–549, https://doi.org/10.1007/s11664-017-5783-3.

[17] Y. Lin, X. Qi, G. Niu, Q. Sun, H. Ji, M. Li, Y. Li, Surface metallization of Si3N4 ceramics with high-performance silver thick paste containing Bi-B-Zn glass frit, J. Mater. Sci. 58 (2023) 9395–9408, https://doi.org/10.1007/s10853-023-08604-2.

[18] Z. Wang, C. Yang, S. Li, Y. Sun, Q. Ma, R. Wang, H. Wang, G. Wang, S. Ma, Study on structure and performance of Bi–B–Zn sealing glass encapsulated Fiber Bragg Grating, Ceram. Int. 49 (2023) 14432–14444, https://doi.org/10.1016/j.ceramint.2023.01.032.

[19] Q. Che, H. Yang, L. Lu, Y. Wang, A new environmental friendly silver front contact paste for crystalline silicon solar cells, J. Alloys Compd. 549 (2013) 221–225, https://doi.org/10.1016/j.jallcom.2012.09.080.

[20] Yang, J., Li, Q., Ding, C., He, L., Xue, L., Cheng, W., Zhang, Z., Wei, G., Liu, Y., Huang, L., Xie, Y., Lu, X., Utilization of $B_2 O_3$ –$Bi_2 O_3$ –ZnO low-temperature glass-ceramics to immobilize iodine-loaded silver-coated silica-gel. J. Mater. Chem. C 9, 10462–10471. https://doi.org/10.1039/D1TC01375K.

[21] J.H. Yang, J.M. Shin, J.J. Park, G.I. Park, M.S. Yim, Novel synthesis of bismuth-based adsorbents for the removal of 129I in off-gas, J. Nucl. Mater. 457 (2015) 1–8, https://doi.org/10.1016/j.jnucmat.2014.09.057.

[22] J.L. Krumhansl, T.M. Nenoff, Hydrotalcite-like layered bismuth–iodine–oxides as waste forms, Appl. Geochem. 26 (2011) 57–64, https://doi.org/10.1016/j.apgeochem.2010.11.003.

[23] Q. Wen, W. Cheng, M. Yan, Y. Liu, Z. Zhang, Y. Xie, D. Shao, X. Lu, Bismuth coordinates with iodine atoms to form chemical bonds for existing stabilization in boron glass, Inorg. Chem. 61 (2022) 9860–9867, https://doi.org/10.1021/acs.inorgchem.1c03680.

[24] S. Cao, C. Guo, Y. Lv, Y. Guo, Q. Liu, A novel BiOCl film with flowerlike hierarchical structures and its optical properties, Nanotechnology 20 (2009) 275702, https://doi.org/10.1088/0957-4484/20/27/275702.

[25] Y. Lei, G. Wang, S. Song, W. Fan, H. Zhang, Synthesis, characterization and assembly of BiOCl nanostructure and their photocatalytic properties, CrystEngComm 11 (9) (2009) 1857–1862, https://doi.org/10.1039/B909013B.

[26] J. Lu, W. Zhou, X. Zhang, G. Xiang, Electronic structures and lattice dynamics of layered BiOCl single crystals, J. Phys. Chem. Lett. 11 (2020) 1038–1044, https://doi.org/10.1021/acs.jpclett.9b03575.

[27] Y. Tian, C.F. Guo, Y. Guo, Q. Wang, Q. Liu, BiOCl nanowire with hierarchical structure and its Raman features, Appl. Surf. Sci. 258 (6) (2012) 1949–1954, https://doi.org/10.1016/j.apsusc.2011.06.137.

[28] Q. Xian, X. Xiao, J. Yu, Y. Gan, L. Chen, X. He, E. Wang, H. Dan, L. Zhu, Y. Ding, T. Duan, High retention immobilization of iodine in b–bi–zn oxide glass using Bi_2O_3 as a stabilizer under a N_2 atmosphere, Inorg. Chem. 61 (2022) 19633–19641, https://doi.org/10.1021/acs.inorgchem.2c03601.

[29] A.J. Lere-Adams, M.C. Dixon Wilkins, D. Bollinger, S. Stariha, R. Farzana, P. Dayal, D.J. Gregg, S. Chong, B.J. Riley, Z.M. Heiden, J.S. McCloy, Glass-bonded ceramic waste forms for immobilization of radioiodine from caustic scrubber wastes, J. Nucl. Mater. 591 (2024) 154938, https://doi.org/10.1016/j.jnucmat.2024.154938.

[30] C26 Committee, Test method for accelerated leach test for diffusive releases from solidified waste and a computer program to model diffusive, fractional leaching from cylindrical waste forms, (n.d.). https://doi.org/10.1520/C1308-08R17.

[31] P.L. Côté, T.W. Constable, A. Moreira, An evaluation of cement-based waste forms using the results of approximately two years of dynamic leaching, Nucl. Chem. Waste Manag. 7 (1987) 129–139, https://doi.org/10.1016/0191-815X(87)90007-6.

[32] Oxford University Press, (54) Plimpton, S. Fast parallel algorithms for short-range molecular dynamics, J. Comput. Phys. 117 (1989) 1–19, https://doi.org/10.1006/jcph.1995.1039, 1995.

[33] M. Parrinello, A. Rahman, Polymorphic transitions in single crystals: a new molecular dynamics method, J. Appl. Phys. 52 (1981) 7182–7190, https://doi.org/10.1063/1.328693.

[34] S. Nose, A unified formulation of the constant temperature molecular dynamics methods, J. Chem. Phys. 81 (1984) 511–519, https://doi.org/10.1063/1.447334.

[35] W.G. Hoover, Canonical dynamics: equilibrium phase-space distributions, Phys. Rev. A 31 (1985) 1695–1697, https://doi.org/10.1103/PhysRevA.31.1695.

[36] Z.Y. Yao, D. Möncke, E.I. Kamitsos, P. Houizot, F. Célarié, T. Rouxel, L. Wondraczek, Structure and mechanical properties of copper–lead and copper–zinc borate glasses, J. Non-Cryst. Solids 435 (2016) 55–68, https://doi.org/10.1016/j.jnoncrysol.2015.12.005.

[37] W. Gao, J. Wang, S. Cao, L. Li, J. Han, Bond characteristics, microstructure, and microwave dielectric properties of Bi2O3–ZnO–B2O3 glass-ceramics with Li2O substitution, Ceram. Int. 50 (2024) 5927–5935, https://doi.org/10.1016/j.ceramint.2023.10.178.

[38] I. Ardelean, S. Cora, V. Ioncu, Structural investigation of CuO-Bi2O3-B2O3 glasses by FT-IR, Raman and UV-VIS spectroscopies. J. Optoelectron, Adv. Mater. 8 (5) (2006) 1843–1847.

[39] W.H. Dumbaugh, Heavy metal oxide glasses containing Bi2O3, Phys. Chem. Glasses 27 (1986) 119–123.

[40] W. Yin, J. Su, M. Cao, C. Ni, S.G. Cloutier, Z. Huang, X. Ma, L. Ren, C. Hu, B. Wei, In (OH)3 and In2O3 micro/nanostructures: controllable NaOAc-Assisted microemulsion synthesis and raman properties, J. Phys. Chem. C 113 (45) (2009) 19493–19499, https://doi.org/10.1021/jp906328z.

[41] M. Jeevaraj, D. Sivaganesh, S. Saravanakumar, S.A. Bahadur, S. Sudhahar, M. K. Kumar, Extrinsic electronic states to tune the luminescence and bonding nature of Cs2NaInCl6 double perovskite, Mater. Chem. Phys. 311 (2024) 128569, https://doi.org/10.1016/j.matchemphys.2023.128569.

[42] A.C. Dakshinamurthy, C. Sudakar, Influence of the octahedral cation on the evolution of lattice phonons in metal halide double perovskites: raman spectroscopic investigation of Cs2B′B″Cl6 (B′= Ag1− x Na x; B ″= Bi 1− x In x), Phys. Rev. Mater. 7 (6) (2023) 065401, https://doi.org/10.1103/PhysRevMaterials.7.065401.

[43] J. Zhang, M. Li, Z. Feng, J. Chen, C. Li, UV Raman spectroscopic study on TiO2. I. Phase transformation at the surface and in the bulk, J. Phys. Chem. B 110 (2) (2006) 927–935, https://doi.org/10.1021/jp0552473.

[44] C. Kranert, R. Schmidt-Grund, M. Grundmann, Raman active phonon modes of cubic In2O3, physica status solidi (RRL)–Rapid Research Letters 8 (6) (2014) 554–559, https://doi.org/10.1002/pssr.201409004.

[45] F. Dong, Y. Sun, M. Fu, Z. Wu, S.C. Lee, Room temperature synthesis and highly enhanced visible light photocatalytic activity of porous BiOI/BiOCl composites nanoplates microflowers, J. Hazard Mater. 219–220 (2012) 26–34, https://doi.org/10.1016/j.jhazmat.2012.03.015.

[46] W. Zhao, L. Li, F. Ling, Y. Wang, G. Xiang, X. Zhou, S. Jiang, Z. Yang, Y. Hua, J. S. Yu, Near-infrared Cr^{3+} -doped lead-free halide perovskite microcrystals for information encryption and temperature thermometry, J. Mater. Chem. C 12 (2024) 4627–4639, https://doi.org/10.1039/D3TC04453J.

[47] G. Li, S. Cheng, X. Chen, M. Wang, F. Zhang, Z. Chen, Y. Liang, X. Li, H. Ji, D. Yang, Y. Han, X. Li, W. Xu, M. Jia, C. Shan, Z. Shi, Erbium-induced boost in self-trapped exciton emission of double perovskites for highly sensitive multimodal and multiplexed optical thermography, Adv. Funct. Mater. (2024) 2403073, https://doi.org/10.1002/adfm.202403073.

[48] C. Khaokhajorn, P. Amornpitoksuk, C. Randorn, T. Rattana, S. Suwanboon, One-pot synthesis of In2O3/ZnO nanocomposite photocatalysts and their enhanced photocatalytic activity against cationic and anionic dye pollutants, Inorg. Chem. Commun. 157 (2023) 111392, https://doi.org/10.1016/j.inoche.2023.111392.

[49] Z. Wan, M. Hu, B. Hu, T. Yan, K. Wang, X. Wang, Vacancy induced photocatalytic activity of La doped In(OH)$_3$ for CO_2 reduction with water vapor, Catal. Sci. Technol. 10 (2020) 2893–2904, https://doi.org/10.1039/D0CY00029A.

[50] S.M. Sze, Y. Li, K.K. Ng, Physics of Semiconductor Devices, John Wiley & Sons, 2021, 2021.

[51] G. Leturcq, A. Grandjean, D. Rigaud, P. Perouty, M. Charlot, Immobilization of fission products arising from pyrometallurgical reprocessing in chloride media, J. Nucl. Mater. 347 (2005) 1–11, https://doi.org/10.1016/j.jnucmat.2005.06.026.

[52] L. Chen, W. Yang, H. Fu, W. Liu, G. Shao, B. Tang, J. Zheng, Mn 2+-doped Cs2NaInCl6 double perovskites and their photoluminescence properties, J. Mater. Sci. 56 (2021) 8048–8059, https://doi.org/10.1007/s10853-021-05822-4.

[53] I.W. Donald, B.L. Metcalfe, S.K. Fong, L.A. Gerrard, D.M. Strachan, R.D. Scheele, A glass-encapsulated calcium phosphate wasteform for the immobilization of actinide-, fluoride-, and chloride-containing radioactive wastes from the pyrochemical reprocessing of plutonium metal, J. Nucl. Mater. 361 (2007) 78–93, https://doi.org/10.1016/j.jnucmat.2006.11.011.

[54] B.J. Riley, D.A. Pierce, J.V. Crum, B.D. Williams, M.M.V. Snyder, J.A. Peterson, Waste form evaluation for RECl3 and REO fission products separated from used electrochemical salt, Prog. Nucl. Energy 104 (2018) 102–108, https://doi.org/10.1016/j.pnucene.2017.09.005.

[55] A. Cozzi, T. Ohji, Environmental Issues and Waste Management Technologies in the Materials and Nuclear Industries XII, John Wiley & Sons, 2009.

[56] B.J. Riley, J.V. Crum, J. Matyáš, J.S. McCloy, W.C. Lepry, Solution-derived, chloride-containing minerals as a waste form for alkali chlorides, J. Am. Ceram. Soc. 95 (2012) 3115–3123, https://doi.org/10.1111/j.1551-2916.2012.05363.x.

[57] E.R. Vance, J. Davis, K. Olufson, I. Chironi, I. Karatchevtseva, I. Farnan, Candidate waste forms for immobilisation of waste chloride salt from pyroprocessing of spent nuclear fuel, J. Nucl. Mater. 420 (2012) 396–404, https://doi.org/10.1016/j.jnucmat.2011.09.020.

[58] W.L. Ebert, Testing to Evaluate the Suitability of Waste Forms Developed for Electrometallurgically Treated Spent sodium-bonded Nuclear Fuel for Disposal in the Yucca Mountain Reporsitory (No. ANL-05/43), Argonne National Lab.(ANL), Argonne, IL (United States), 2006, https://doi.org/10.2172/881577.

[59] W.L. Ebert, C.T. Snyder, S. Frank, B. Riley, Designing advanced ceramic waste forms for electrochemical processing salt waste. https://doi.org/10.2172/1326909, 2016.

[60] B.J. Riley, Electrochemical salt wasteform development: a review of salt treatment and immobilization options, Ind. Eng. Chem. Res. 59 (21) (2020) 9760–9774, https://doi.org/10.1021/acs.iecr.0c01357.

[61] F. Angeli, P. McGlinn, P. Frugier, Chemical durability of hollandite ceramic for conditioning cesium, J. Nucl. Mater. 380 (2008) 59–69, https://doi.org/10.1016/j.jnucmat.2008.07.003.

[62] W.E. Lee, M.I. Ojovan, M.C. Stennett, N.C. Hyatt, Immobilisation of radioactive waste in glasses, glass composite materials and ceramics, Adv. Appl. Ceram. 105 (2006) 3–12, https://doi.org/10.1179/174367606X81669.

[63] M.I. Ojovan, G.A. Varlackova, Z.I. Golubeva, O.N. Burlaka, Long-term field and laboratory leaching tests of cemented radioactive wastes, J. Hazard Mater. 187 (2011) 296–302, https://doi.org/10.1016/j.jhazmat.2011.01.004.

[64] A.S. Wagh, S.Y. Sayenko, V.A. Shkuropatenko, R.V. Tarasov, M.P. Dykiy, Y. O. Svitlychniy, V.D. Virych, E.A. Ulybkina, Experimental study on cesium immobilization in struvite structures, J. Hazard Mater. 302 (2016) 241–249, https://doi.org/10.1016/j.jhazmat.2015.09.049.

[65] K. Yanagisawa, M. Nishioka, N. Yamasaki, Immobilization of cesium into pollucite structure by hydrothermal hot-pressing, J. Nucl. Sci. Technol. 24 (1987) 51–60, https://doi.org/10.1080/18811248.1987.9735774.

[66] M.L. Carter, A.L. Gillen, K. Olufson, E.R. Vance, HIPed tailored hollandite waste forms for the immobilization of radioactive Cs and Sr, J. Am. Ceram. Soc. 92 (2009) 1112–1117, https://doi.org/10.1111/j.1551-2916.2009.03021.x.

[67] V. Luca, E. Drabarek, C.S. Griffith, H. Chronis, J. Foy, The immobilization of cesium and strontium in ceramic materials derived from tungstate sorbents, MRS Online Proc. Libr. 807 (2003) 303, https://doi.org/10.1557/PROC-807-303.

[68] M. Zhao, Y. Xu, L. Shuller-Nickles, J. Amoroso, A.I. Frenkel, Y. Li, W. Gong, K. Lilova, A. Navrotsky, K.S. Brinkman, Compositional control of radionuclide retention in hollandite-based ceramic waste forms for Cs-immobilization, J. Am. Ceram. Soc. 102 (2019) 4314–4324, https://doi.org/10.1111/jace.16258.

[69] W.L. Ebert, J.A. Fortner, Corrosion Tests with Developmental Iron Phosphate Glass Waste Forms (No. ANL/CFCT-19/7), Argonne National Lab.(ANL), Argonne, IL (United States), 2019.

[70] A. Ivanets, I. Shashkova, N. Kitikova, et al., Enhanced adsorption to safe immobilization of cesium radionuclides, J. Radioanal. Nucl. Chem. 334 (1) (2025) 315–327, https://doi.org/10.1007/s10967-024-09779-x.

[71] O.O. Shichalin, E.K. Papynov, A.A. Belov, et al., Immobilization of 137Cs in NaY type zeolite matrices using various heat treatment methods, Solid State Sci. 154 (2024) 107619, https://doi.org/10.1016/j.solidstatesciences.2024.107619.

[72] A. Ivanets, A. Dzikaya, I. Shashkova, et al., Utilization of (Ca, Mg)-Zr phosphates adsorbents saturated by Cs+, Sr2+, Co2+ ions in NZP ceramic matrices, J. Eur. Ceram. Soc. 44 (13) (2024) 7716–7729, https://doi.org/10.1016/j.jeurceramsoc.2024.05.030.

[73] E.K. Papynov, O.O. Shichalin, I.Y. Buravlev, et al., Preparation of pollucite ceramic matrices as 137Cs ionizing radiation source by spark plasma sintering, Ceram. Int. 50 (2) (2024) 2759–2771, https://doi.org/10.1016/j.ceramint.2023.10.341.